Molecular Dynamics Simulation of Macromolecular Interactions in Solution: Poly(γ-benzyl glutamate) in Dimethylformamide and Tetrahydrofuran

J. Helfrich and R. Hentschke*

Max-Planck-Institut für Polymerforschung, Postfach 3148, 55021 Mainz, Germany

Received December 5, 1994; Revised Manuscript Received March 23, 1995[⊗]

ABSTRACT: We carry out molecular dynamics simulations of the interaction between pairs of short segments of poly(γ-benzyl glutamate) in dimethylformamide and in tetrahydrofuran as a function of molecular orientation and separation in the range between ~1 and ~3 nm. We find that the solvation shell structure induced by poly(γ-benzyl glutamate) in the surrounding solvent plays a significant role for the molecular interaction in solution. In particular, as in the case of macroscopic solid−liquid−solid interfaces, we show that the intersegment force shows a pronounced oscillatory behavior depending on the commensurability of the intersegment separation with the solvation shell structure. We also find a pronounced dependence of the force on the molecular orientation as well as on the type of solvent.

1. Introduction

The interaction of large rodlike molecules in solution is governed by a whole hierarchy of interactions becoming important on different length scales. Upon increasing the concentration, the molecules are subject to excluded-volume interactions for which the molecular contour length sets the scale. In more concentrated solutions, rodlike molecules tend to align (e.g., ref 1), and, since they are usually flexible, they experience a reduction of their conformational entropy because of the suppression of their undulatory freedom due to the presence of their neighbors.[2] The distance dependence of this type of interaction is governed by a power law decay if the molecules can be considered as being confined to a hard tube of neighbors.[2−4] At even higher concentrations, when the molecules are strictly aligned, their solvation shells begin to interact, where the range of this interaction usually is on the order of several solvent molecule diameters (e.g., ref 5 and references therein). After the solvent is squeezed out between the rodlike molecules, usually the steric repulsion between them dominates. This, of course, is a very much simplified scenario. Many rodlike molecules are polyelectrolytes or, in order to promote solubility, are surrounded by dense "brushes" of side chains mixing with the solvent. In the case of polyelectrolytes the decay length of the electrostatic double-layer interaction is the Debye length, which depends, for instance, on ionic strength. In the case of side-chain interactions, on the other hand, it is, of course, the extension of the side chains which is important. The picture gets even more complicated since the various contributions may couple. For instance, flexibility and double-layer interactions must be combined to explain the solute and salt concentration dependence of osmotic pressure data in highly concentrated solutions of DNA, and the typical decay length for the combined interaction is again different.[5,6] Thus, studying the interactions between macromolecules in solution is an interesting topic, because these forces form the basis of many complex liquid-crystalline or crystalline types of ordering. The complexity of the interactions make atomistic computer simulations a potentially useful tool in this context. However, one always must emphasize that, for instance, with a molecular dynamics simulation on the atomic level we still are limited to fairly small system sizes (on the order of 70−90 Å in the present case) and thus we only can hope to model a small portion of the above interactions.

As an example of a simulation of effective intermolecular forces in solution, we chose to study the interaction between pairs of short segments of one particular molecule, i.e., poly(γ-benzyl glutamate) (PBG), in two different solvents, i.e., dimethylformamide (DMF) and tetrahydrofuran (THF), as a function of the molecular separation and orientation. The choice of this system is motivated by its frequent use in the contexts of lyotropic liquid-crystalline behavior[7−13] as well as the formation of highly ordered films on surfaces.[14] In addition, this paper is a sequel to a previous molecular dynamics simulation study focused mainly on the behavior of a single poly(γ-benzyl L-glutamate) (PBLG) molecule in solution.

More precisely, we first carry out PBG/DMF simulations of the interaction between two helical PBG molecules in DMF, where the intermolecular separation ranges from ~1 to ~3 nm. We consider two different systems with "extreme" configurations of the interacting PBG segments. In system I both segments are oriented parallel, whereas in system II they are oriented perpendicular to each other. Previously, we found that the PBG molecule induces an extensive solvation structure in the surrounding solvent, which has an approximate diameter of 30 Å. In the crystalline state, on the other hand, X-ray studies show that the intermolecular spacing is only about 15.6 Å. Simulating the interactions in the parallel configuration (I), we find a noticeable onset of repulsive interactions at ~18.5 Å, which still is significantly larger than the crystalline diameter and thus underscores the importance of the solvent for the interaction. In addition, we find that the force in this configuration is purely repulsive, with oscillations caused by the restructuring of the solvation zone between the molecules. This is analogous to what one usually observes in surface force apparatus experiments on macroscopic solid-to-liquid-to-solid interfaces.[15] Thus, we are essentially simulating a molecular surface force apparatus. In comparison, the crossed geometry of system II produces both attractive as well as repulsive interactions depending on the molecular separation. Finally, we consider a third system (III), which is

[⊗] Abstract published in *Advance ACS Abstracts,* May 1, 1995.

0024-9297/95/2228-3831$09.00/0

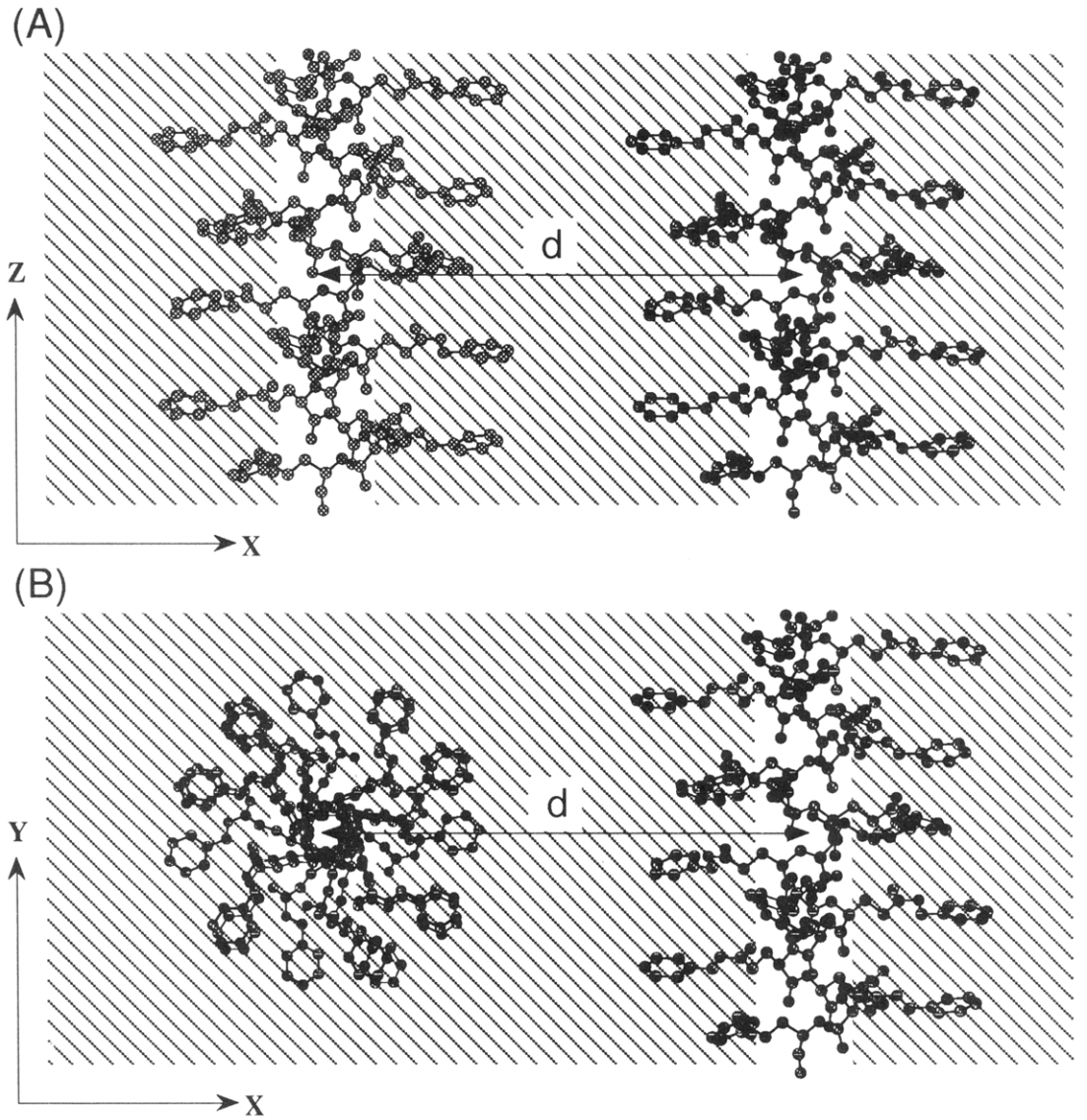

Figure 1. Schematic illustration of the constructed systems. (A) Side view onto the xz-plane of systems I and III: Two helical PBG molecules are placed parallel to the z-axis into the surrounding solvent separated by a distance d. The PBG molecules are shown in a ball-and-stick representation, whereas the solvent molecules are represented by the shading. (B) Top view onto the xy-plane of system II: The two PBG molecules are oriented parallel to the z- and y-axes, respectively.

identical to system II except that DMF is replaced by THF. Here we find that the solvation shell structure induced by PBLG in THF is much more pronounced. Correspondingly, we find noticeable differences in the force vs distance relation in this system in comparison to system I.

The paper is structured as follows. The first three sections discuss the construction of the simulated systems, the employed force field, and the methodology of the intersegment force calculations. The next three sections are devoted to the results obtained for the three different systems, i.e., PBG in DMF with parallel segments (I), PBG in DMF with perpendicular segments (II), and PBG in THF again with parallel segments (III). The last section is the conclusion.

2. Method

2.1. Construction of the Simulated Systems. The helical PBG segments, which we use in our present simulations, are constructed according to ref 16. Their initial conformation is an instantaneous conformation extracted from our previous simulation after approximately 1 ns.[17] Along the axial direction we repeat the helix segments periodically via covalent bonds between the real and the image segments.

In system I two PBG helix segments, which are 18_5 α-helices with an axial rise per repeat unit of 1.5 Å, are placed parallel to the z-axis into a rectangular box of volume $V = L_x L_y L_z$. The initial separation of the helices along the x-axis is ~22 Å (cf. Figure 1A). Notice that the second helix segment initially is created as a mirror image of the first segment, which, of course, changes the handedness of the second segment with respect to the first. Here the first segment is a PBLG segment, whereas the second segment thus is a poly(γ-benzyl D-glutamate) (PBDG) segment. Clearly, this is a special case, corresponding to a "racemic mixture". However, it is worth pointing out that the equation of state of PBLG can be described quite well using simple excluded-volume models, which do not account for the helical nature of the molecules.[7] Thus we expect the effect of the helical "corrugation" of the molecules on the overall forces to be small (cf. below). The box length along the z-direction, L_z = 27.04 Å, corresponds to the repeat distance of the PBLG helix,[17] whereas the dimensions along the x- and y-directions are determined by the

range of the solvent structure, which is induced by the two PBG segments. Therefore, we choose a box length in the x-direction that exceeds the range of the side chains of one single PBG helix by about a factor of 4, whereas in the y-direction the box length exceeds the range of the side chains approximately twice. Note that this difference is due to the fact that we want to vary the segment-to-segment separation along x. The DMF molecules initially are placed on a regular lattice inside the simulation box surrounding the PBG segments according to the DMF bulk density $\varrho_{DMF} = 0.944$ g cm^{-3} at 300 K[18] as described previously.[17] The equilibration of the thus constructed system is carried out via a subsequent molecular dynamics run, where we additionally compress the simulation box in the x-direction by 0.2% in order to achieve bulk density in the vicinity of the box boundaries. The final simulation box has the lateral dimensions $L_x = 94.9$ Å, $L_y = 60$ Å, and $L_z = 27.04$ Å and contains 1144 DMF molecules (i.e., a total of 14 772 atoms).

In system II, the two helices are both PBLG and they are in a crossed configuration; i.e., one helix is oriented parallel to the y-axis and the second helix is oriented parallel to the z-axis. Here the centers of mass of the PBLG molecules are initially separated along the x-axis by ~21 Å. This configuration is created by translating a duplicate of the first segment along x and rotating it by $\pi/2$. Note that for this cross-like geometry the box lengths in the y-direction as well as in the z-direction are determined by the repeat distance of the constructed PBLG segments. In order to prevent the interaction with the periodic images, in this configuration, we construct two helices consisting of 36 monomers each so that $L_y = L_z = 54.08$ Å, which is twice the repeat distance. The dimension in the x-direction $L_x = 63.8$ Å, is chosen according to the requirement of bulklike behavior at the box boundaries as discussed for system I. Here the final simulation box contains 1320 DMF molecules (i.e., a total of 17 928 atoms) and is schematically illustrated in Figure 1B.

System III corresponds to system I, where now DMF is replaced by THF. Thus the simulation box contains 1136 THF molecules and two PBG segments, which are oriented parallel to the z-direction (i.e., a total of 15 812 atoms). As in system I the lateral dimensions of the simulation box in the y- and z-directions are $L_y = 60$ Å and $L_z = 27.04$ Å, whereas the box length in the x-direction is again adjusted to yield the proper THF bulk density $\varrho_{THF} = 0.873$ g cm^{-3} at 300 K,[18] which leads to $L_x = 98.2$ Å.

For the single-segment simulation, which additionally is included in this case (cf. below), we construct a simulation box, which contains only one single PBLG segment equivalent to the PBLG/DMF system described previously.[17] Here, a PBLG segment consisting of 18 monomers is centered parallel to the z-axis in a box with the lateral dimensions $L_x = L_y = 70.5$ Å and $L_z = 27.04$ Å. This simulation box contains 1135 THF molecules (i.e., a total of 15 799 atoms).

Because of the large number of atoms contained in these various systems, a fully atomistic molecular dynamics simulation would require excessive computer time. In order to reduce the computational effort, we apply the "united atom" model; i.e., explicit CH−, CH$_2$−, or CH$_3$− groups are replaced by effective single carbon atoms with correspondingly increased atomic mass and van der Waals radius. Thus, the total number of simulated atoms is decreased to 6332 atoms in system I, to 7824 atoms in system II, to 6292 atoms in system III, and to 6287 atoms in the single-segment PBLG/THF simulation.

2.2. Force-Field and Simulation Methodology. The MD simulations are based on the numerical integration of Newton's equations of motion

$$m_i \frac{d^2\vec{x}_i}{dt^2} = -\vec{\nabla}_{\vec{x}_i} V(\vec{x}_1,...,\vec{x}_n) \tag{1}$$

where i runs over all n (united) atoms in the simulation box. The simulations are carried out using the molecular mechanics and molecular dynamics modules provided in the AMBER (Assisted Model Building with Energy Refinement) molecular modeling package, where $V(\vec{x}_1,...,\vec{x}_n)$ is given by

$$V = \sum_{\text{bonds}} f_r(r - r_{\text{equ}})^2 + \sum_{\text{valence angles}} f_\delta(\delta - \delta_{\text{equ}})^2 + \sum_{\text{dihedrals}} f_n[1 + \cos(n\phi - \gamma)] + \sum_{i<j}\left(\frac{A_{ij}}{r_{ij}^{12}} - \frac{B_{ij}}{r_{ij}^{6}}\right) + \sum_{i<j}\frac{q_i q_j}{r_{ij}} + \sum_{\text{H-bonds}}\left(\frac{C_{ij}}{r_{ij}^{12}} - \frac{D_{ij}}{r_{ij}^{10}}\right) \tag{2}$$

$$A_{ij} = \sqrt{\epsilon_i \epsilon_j}(\sigma_i + \sigma_j)^{12}$$

$$B_{ij} = 2\sqrt{\epsilon_i \epsilon_j}(\sigma_i + \sigma_j)^{6}$$

The first three terms describe bonding interactions (due to bond, valence angle, and dihedral deformations). The remaining nonbonding terms are Lennard-Jones (LJ) interactions (using the Lorentz−Berthelot mixing rule[19] to obtain the LJ parameters, i.e., the usual LJ potential parameters ϵ_{ij} and σ_{ij} are expressed as $\epsilon_{ij} = \sqrt{\epsilon_i \epsilon_j}$ and $\sigma_{ij} = \sigma_i + \sigma_j$, where the indices label the interacting atoms and a factor of 0.5 has been absorbed into σ_i and σ_j), Coulomb interactions, and hydrogen bond interactions. Note that all LJ and Coulomb 1−4 nonbonded interactions (i.e., interactions between atoms separated by three bonds) are scaled by a factor of 0.5.[20] The atomic partial charges are calculated using the charge equilibration algorithm[21] as provided in the software package POLYGRAF.[22] Note that with the so-calculated partial charges we previously[17] obtained a (united atom) dipole moment $\mu = 3.27$ D for DMF, which is in excellent agreement with the experimental value $\mu_{exp} = 3.24$ D.[18] The analogous procedure applied to THF yields a (united atom) dipole moment of $\mu = 1.75$ D, which also is in quite reasonable agreement with the experimental value of $\mu_{exp} = 1.95$ D.[18] The PBG/DMF force-field parameters are compiled in Table 1 of ref 17. (Note that erroneously in this table we omitted the values for the H-bond parameters, which are the AMBER values $C = 7557$ kcal/mol·Å^{-12} and $D = 2385$ kcal/mol·Å^{-10} taken from ref 20.) In this work we use the previous parameters with the exception of the united atom DMF-carbon LJ parameters, as we will discuss in the next section. The new DMF-carbon LJ parameters as well as the additional PBG/THF parameters are compiled in Table 1.

During the MD simulations all nonbonded interactions are omittec beyond a residue-based cutoff of 8 Å; i.e., the complete interactions between two residues are calculated if any two atoms of the respective residues are closer than the cutoff. In the case of the parallel

Table 1. Partial Charges and New LJ Parameters for DMF and THF[a]

Partial Charges

DMF		q (electron charges)	THF		q (electron charges)
	C_0	0.51		O	−0.54
	O	−0.48		C_1	0.28
	N	−0.39		C_2	−0.02
	C_1	0.12		C_3	−0.01
	C_2	0.24		C_4	0.28

LJ Parameters

DMF	ϵ (kcal mol^{-1})	σ (Å)	THF	ϵ (kcal mol^{-1})	σ (Å)
C3	0.143 (0.15)	2.172 (2.0)	C2	0.09 (0.12)	2.15 (1.925)

[a] The partial charges are calculated via the charge equilibration algorithm,[21] which is part of the POLYGRAF[22] modeling package. A complete compilation of the force-field parameters, which are basically adapted from the AMBER data base,[20] is given in ref 17. Here we present only modified LJ parameters, where we used the AMBER atom type convention: C2 = carbon with two hydrogens, C3 = carbon with three hydrogens. The parameters in brackets represent the original AMBER parameters.

geometry (systems I and III), the residues are the entire PBG segments and the individual solvent molecules, respectively. In the case of the perpendicular geometry (system II), on the other hand, the residues are the PBG repeat units and the individual solvent molecules. Keeping the bond lengths fixed using the SHAKE algorithm,[23] the atomic equations of motion are solved using a leap-frog version of the Verlet algorithm with a 5 fs time step for the PBG/DMF systems. When THF is used as solvent, a 5 fs time step proved to be too inaccurate, and shorter time steps of 3 and 2 fs were used in the double- and single-segment simulations, respectively. A constant temperature is maintained according to the method of Berendsen et al.[24] using velocity rescaling with a temperature relaxation time of 0.1 ps.

2.3. Solvent Characterization. As mentioned before, throughout the current work the solvent molecules are described in terms of the united atom model, which means that CH−, CH_2−, and CH_3− groups are replaced by single effective carbon atoms with adjusted interaction parameters. This approximation sensitively influences the molecule excluded volume and therefore the solvent dynamics. To check the solvent united atom parameters, which were taken from the AMBER data base, we perform separate *NVT* simulations for each solvent. The simulations are carried out at 300 K with a 2 fs time step and a 8 Å cutoff (the sizes of the cubic simulation boxes are chosen according to the experimental bulk densities).

We characterize the solvent dynamics by calculating the bulk self-diffusion coefficient via the Einstein relation

$$D = \lim_{t\to\infty} \frac{1}{6}\frac{\partial}{\partial t}\langle \Delta \vec{r}_i{}^2 \rangle_{i,t_0} \qquad (3)$$

where $\Delta\vec{r}_i$ is the displacement of solvent molecule i during the time interval t. The average is taken over all molecules i contained in the simulation box as well as with respect to different time origins t_0 along the simulation trajectory.

The parameters for DMF as well as its diffusion coefficient were already presented in ref 17. However, regretfully we discovered an error in the calculation of the diffusion coefficient. A recalculation with the previous data leads to a bulk diffusion coefficient of $D = 3.3 \times 10^{-9}$ m^2/s instead of 2.2×10^{-9} m^2/s, whereas the experiment predicts a value of $D_{exp} = 1.98 \times 10^{-9}$ m^2/s. To rectify this discrepancy, we increased the united atom van der Waals radius of the DMF methyl groups by approximately 5% beyond its AMBER value. As a result we obtain a diffusion coefficient of $D = 2.0 \times 10^{-9}$ m^2/s, which is in good agreement with the experimental value $D_{exp} = 1.98 \times 10^{-9}$ m^2/s. A plot of the mean-square displacement divided by 6 vs time is shown in Figure 2. We also checked the influence of the increased van der Waals radius on our other previously obtained results. We find that the structural properties are not noticeably affected by the small change in the C3 van der Waals parameters and that no further corrections of the previous results are necessary. The final LJ parameters for C3 are compiled in Table 1.

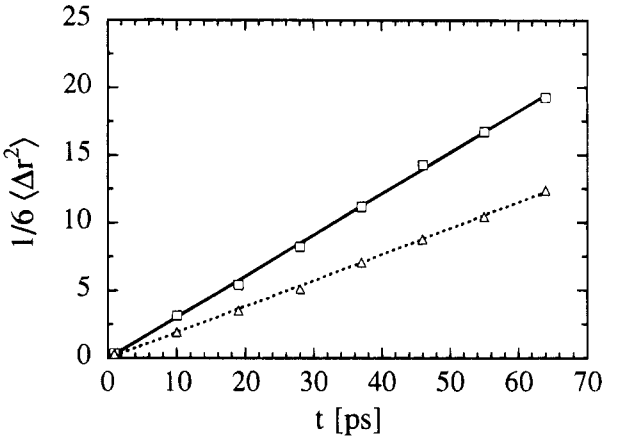

Figure 2. Mean-square displacement $\langle \Delta r^2 \rangle$ divided by 6 vs time t for DMF (△) and THF (□). A linear fit yields the bulk diffusion coefficient for DMF, i.e., $D = 2 \times 10^{-9}$ m^2/s (dotted line), and for THF, i.e., $D = 3.1 \times 10^{-9}$ m^2/s (solid line), which has to be compared with the experimental values $D_{DMF} = 1.98 \times 10^{-9}$ m^2/s and $D_{THF} = 3.4 \times 10^{-9}$ m^2/s, respectively.

In the case of THF we also find that the AMBER united atom parameters are not satisfactory and the simulated THF shows a nonliquidlike behavior. As before for DMF we therefore increase the van der Waals radius of the THF C2 atoms and compare the resulting diffusion coefficient with the proper experimental value. Figure 2 shows the THF mean-square displacement divided by 6 as a function of time for the adjusted LJ parameters, which are compiled together with the original AMBER parameter set in Table 1. The diffusion coefficient, calculated via a linear fit is $D = 3.1 \times 10^{-9}$ m^2/s, which has to be compared with the experimental value of $D_{exp} = 3.4 \times 10^{-9}$ m^2/s.[25]

The difference in bulk liquid structure between DMF and THF is shown in Figure 3 in terms of the pair correlation functions $g(r') = \langle \varrho^*(0))\, \varrho^*(r') \rangle$, where $\varrho^*(r') = \varrho(r')/\varrho_{bulk}$ and $\varrho(r')$ is the local liquid density. In the case of DMF the profile exhibits a first peak at $r' = 5.2$ Å, which specifies the separation of the nearest neighbors, and a less pronounced second peak at $r' = 9.5$ Å, indicating the second shell of neighbors. The THF pair correlation function displays a more strongly pronounced structure with clearly discernible oscillations out to ~13 Å, where the first peak is at $r' = 5.5$ Å and the second peak appears at $r' = 9.8$ Å. Interestingly, in spite of the larger dipole moment of DMF $\mu_{DMF} = 3.24$ D ($\mu_{THF} = 1.95$ D), the ordering of the DMF solvent molecules is less pronounced, indicating that the higher

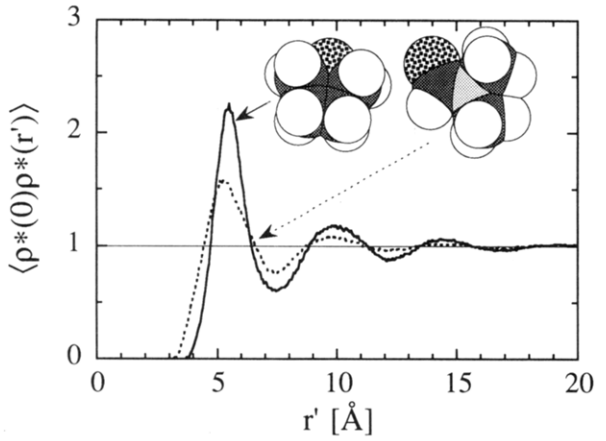

Figure 3. Center of mass pair correlation functions for DMF (dotted line) and THF (solid line) where r' denotes the intermolecular separation. In addition, the two molecules are shown as space-filling models (dark shading indicates carbons; dotted spheres indicate oxygen).

symmetry of the ringlike THF molecule significantly influences the solvent's short-range order.

2.4. Calculation of the Intersegment Forces. To determine the interaction force between two helical PBG segments in solution, we calculate the external constraining force, which must be applied to the PBG backbone in order to keep the segments at a specific separation. The external force thus applied to the backbones mirrors directly the repulsion/attraction of the segments and therefore provides detailed insight into the effective PBG–PBG interaction in solution.

To control the segment separation, certain backbone atoms in one PBG segment are linked to the corresponding atoms in the other segment through additional "virtual" bonds. During the dynamic simulation of the segments at a specified separation the lengths of the virtual bonds are kept constant by the constraining forces, which are introduced into the equations of motion of the backbone atoms. The described linking of the backbone atoms is illustrated schematically in parts A and B of Figure 4 for both the parallel and the perpendicular segment geometries. In systems I and III, i.e., when the segments are parallel, the peptide backbone atoms of the first PBG molecule are linked with the respective opposite lying backbone atoms of the second PBG molecule through the virtual bonds (cf. the dotted lines in Figure 4A). The virtual bond lengths are calculated during the first simulation step and subsequently are kept constant by the constraining forces throughout the simulation (at this particular segment-to-segment separation). In system II, where the two PBG segments are oriented perpendicular to each other, the geometrical configuration makes a direct virtual connection of the respective backbone atoms in the two segments inconvenient. For this reason we take the initial configuration (at $t = 0$) of the helical backbones as two static reference segments, which remain unchanged during the course of the simulation, and connect the peptide backbone atoms of the simulated PBG segments with the corresponding atoms of its reference segment (cf. Figure 4B).

Note in this context that the PBG α-helix is stabilized by the formation of hydrogen bonds whose geometry and dynamics we already discussed in ref 17. To avoid the disturbance of the hydrogen bond structure along the backbone, we do not introduce virtual bonds involving peptide hydrogen atoms. Thus, only the nitrogen,

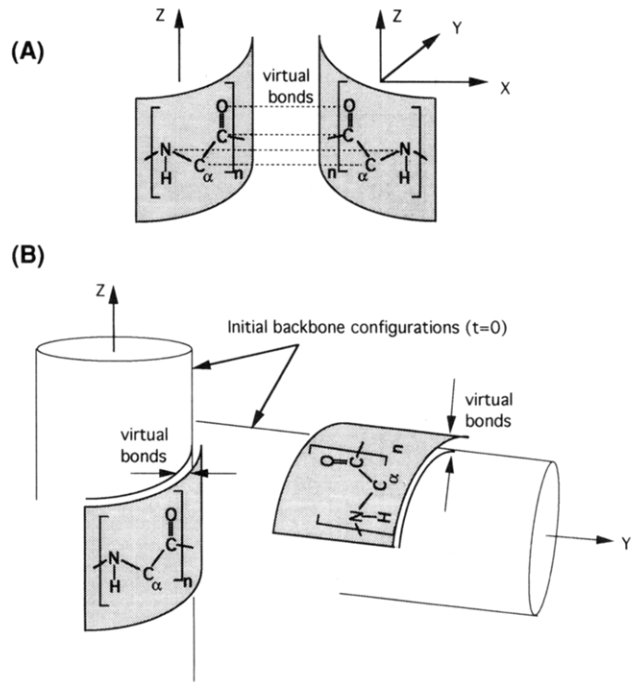

Figure 4. Schematic illustration of the virtual bonds. (A) Two parallel helices: All backbone atoms (except for the hydrogens) are linked through virtual bonds with the respective atoms of the opposite backbone. (B) Two perpendicular helices: The atoms of each backbone (except for the hydrogens) are linked with their initial position at $t = 0$.

carbon, and oxygen atoms along the backbone are subjected to the constraints, whereas the peptide hydrogen atoms retain their full dynamical freedom.

All atoms linked by virtual bonds move according to their normal inter- and intramolecular interactions. Their positions are corrected only if the deviation from the preassigned virtual bond length exceeds a certain margin. The applied correction procedure is similar to the SHAKE algorithm,[23] which is commonly used to fix the "real" covalent bond lengths within the molecules. The following description of the correction algorithm is based on the virtual bond geometry of the systems I and III (cf. Figure 1A), but it can also be transferred straightforwardly to system II.

The equation of motion for two backbone atoms labeled 1 and 2 connected by a virtual bond of length d_{12} (note that the atoms belong to different segments) can be written as

$$m \frac{\partial^2}{\partial t^2} \vec{r}_i = \vec{f}_i + \vec{g}_i \; (i = 1, 2) \tag{4}$$

where $\vec{r}_i$ is the position of atom i, $\vec{f}_i$ is the total force acting on atom i resulting from the inter- and intramolecular interactions, and $\vec{g}_i$ is the force necessary to fulfill the condition

$$d_{12} = |\vec{r}_1(t) - \vec{r}_2(t)| = |\vec{r}_{12}(t)| = \text{const} \tag{5}$$

for all t. We can now write

$$\vec{r}_i(t+\delta t) = \vec{r}_i'(t+\delta t) + \Delta\vec{r}_i(t) \tag{6}$$

with

$$\Delta\vec{r}_i(t) = \frac{(\delta t)^2}{m}\vec{g}_i(t)$$

where $\vec{r}_i'$ is the solution of (4) for $\vec{g}_i = 0$, and δt is the integration step size. The correction $\Delta\vec{r}_i$ has to ensure that the equation

$$|\vec{r}_{12}(t+\delta t)| = |\vec{r}_{12}(t)| \tag{7}$$

is satisfied for all t.

The forces $\vec{g}_i$ acting on the backbone atoms are directed along the additional virtual bonds and thus can be written as

$$\vec{g}_1 = \lambda_{12}\vec{r}_{12}(t) \qquad \vec{g}_2 = -\lambda_{12}\vec{r}_{12}(t) \tag{8}$$

where λ_{12} is an undetermined Lagrange multiplier. Inserting (8) into (6) and subtracting the corrected positions of atom 1 and atom 2, one obtains

$$\vec{r}_{12}(t+\delta t) = \vec{r}_1'(t+\delta t) - \vec{r}_2'(t+\delta t) + 2\frac{(\delta t)^2}{m}\lambda_{12}\vec{r}_{12}(t)$$

$$= \vec{r}_{12}'(t+\delta t) + 2\frac{(\delta t)^2}{m}\lambda_{12}\vec{r}_{12}(t) \tag{9}$$

The square modulus of both sides leads to the expression

$$|\vec{r}_{12}(t+\delta t)|^2 = |\vec{r}_{12}'(t+\delta t)|^2 + 4\frac{(\delta t)^2}{m}\lambda_{12}\vec{r}_{12}(t)\,\vec{r}_{12}'(t+\delta t) + 4\frac{(\delta t)^4}{m^2}\lambda_{12}^2|\vec{r}_{12}(t)|^2 \tag{10}$$

Applying the constraint (7) and neglecting the term of order $(\delta t)^4$, (10) becomes

$$d_{12}^2 = |\vec{r}_{12}'(t+\delta t)|^2 + 4\frac{(\delta t)^2}{m}\lambda_{12}\vec{r}_{12}(t)\,\vec{r}_{12}'(t+\delta t) \tag{11}$$

which can be solved for λ_{12}, i.e.

$$\lambda_{12} = \frac{d_{12}^2 - |\vec{r}_{12}'(t+\delta t)|^2}{4\frac{(\delta t)^2}{m}\vec{r}_{12}(t)\,\vec{r}_{12}'(t+\delta t)} \tag{12}$$

Thus using (8) and (12), the correction of the atomic positions $\Delta\vec{r}_i$ in (6) is given by

$$\Delta\vec{r}_1 = \frac{1}{4}\frac{d_{12}^2 - |\vec{r}_{12}'(t+\delta t)|^2}{\vec{r}_{12}(t)\,\vec{r}_{12}'(t+\delta t)}\vec{r}_{12}(t) \qquad \Delta\vec{r}_2 = -\Delta\vec{r}_1 \tag{13}$$

Finally, using (12) and (13) the constraining forces (8) acting on the atoms $i = 1, 2$ in order to keep the bond length d_{12} constant take on the form

$$\vec{g}_i(t) = \frac{m}{4(\delta t)^2}\Delta\vec{r}_i \; (i = 1, 2) \tag{14}$$

Note that a positive force represents a repulsion and a negative force an attraction of the connected atoms. In order to minimize the influence of the introduced backbone constraints on the internal motion of the backbone itself, the virtual interhelical bond lengths d_{ij} are allowed to fluctuate about their assigned value $\bar{d}_{ij}$ by ±1 Å; i.e., a force is applied only if the value of $|\vec{r}_i(t) - \vec{r}_j(t)|$ exceeds the allowed boundaries $\bar{d}_{ij} \pm 1$ Å. As mentioned before, only backbone atoms are subjected to these additional constraints, whereas the PBG side chains as well as the solvent atoms retain their full dynamical freedom.

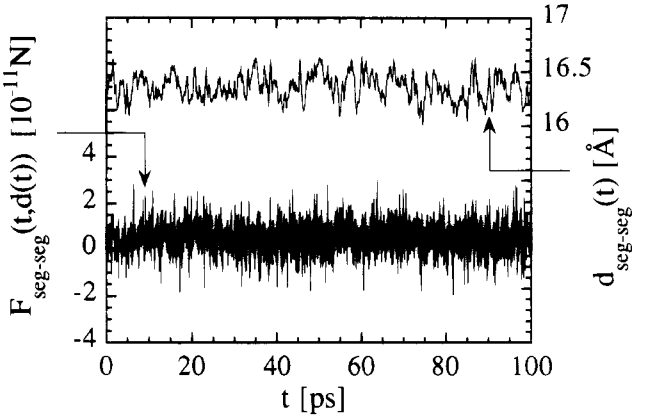

Figure 5. Typical simulation results obtained in the case of two parallel PBG segments in DMF initially separated by 16.3 Å: Total force $F_{seg-seg}(t,d(t))$ acting on the backbone of a segment along the perpendicular connection between the centers of mass of the two segments (lower curve) and corresponding center of mass distance $d(t)$ (upper curve) as a function of simulation time t. The allowed virtual bond length fluctuation is ±1 Å.

To calculate the forces $\vec{g}_i$ as a function of the segment separation d, we produce several system conformations with different interhelix separations according to the following procedure. The initial system is preequilibrated during a 300 ps *NVT* dynamics run at 300 K. In the cases of the systems I and III, we subsequently perform a short simulation run, where we continuously lower the virtual bond lengths by a small amount at each integration step. The slow change of the virtual bond lengths cause the helices to move through the surrounding solvent to the various positions at which we subsequently want to measure the force. In order to produce corresponding startup conformations for system II, we kept the virtual bond lengths fixed and slowly let the reference segments approach each other along the x-direction. Because of the connection between the PBG helices and their corresponding reference segments, we again achieve a continuous decrease of the helix-to-helix separation. As before we extract the system configurations which we later use as starting configurations for the force measurements at constant d at regular intervals $\Delta d = 1$ Å. On the basis of each starting configuration for a specific d, we perform 200 ps *NVT* dynamic runs applying the above method to measure the forces $\vec{g}_i$, which are extracted from the last 100 ps of each run. Note that perpendicular to the direction which connects the segment centers of mass (cf. Figure 1) the forces vanish on average. Therefore, we only consider the force component along the x-direction and compute the total force between the segments $F_{seg-seg}(t,d(t))$ by summing the x-components of the $\vec{g}_i$.

Figure 5 illustrates the typical time behavior of the PBG center of mass separation $d(t)$ as well as the intersegment force $F_{seg-seg}(t,d(t))$ obtained for system I, where the two parallel helices are initially separated by $\bar{d} = 16.3$ Å. Note that the standard deviation of the PBG separation is ~0.12 Å, whereas a standard deviation of $\sim 0.7 \times 10^{-11}$ N is obtained for the intersegment force. In the following discussions we characterize each simulation during which the intersegment separation is constrained by an average helix-to-helix distance d and a corresponding average intersegment force $F_{seg-seg}(d)$ obtained from the time averages of $d(t)$ and $F_{seg-seg}(t,d(t))$, respectively.

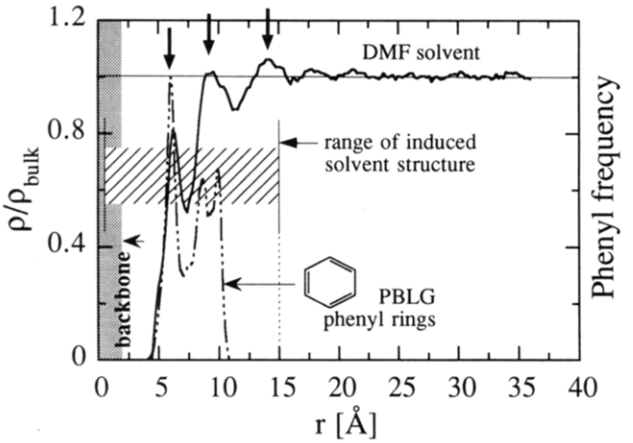

Figure 6. DMF solvent density ϱ divided by the bulk density ϱ_{bulk} as a function of the radial distance r from the helix axis (solid line) and radial center of mass distribution of the PBG phenyl rings (dash-dotted line) obtained from a molecular dynamics simulation of a single PBLG molecule in DMF. The striped horizontal bar indicates the range of the induced solvent structure, which includes ~3 solvent shells indicated by the arrows. Note that the gray-shaded area labeled "backbone" denotes the radial extension of the PBG backbone.

3. Forces between Parallel PBG Segments in DMF and THF

3.1. Two Parallel PBG Segments in DMF. Previously[17] we carried out molecular dynamics simulations to characterize the solvent side-chain interface of a single PBLG molecule in DMF. Figure 6 shows the resulting radial center of mass density of DMF as a function of the radial distance r from the helix axis. The peaks in the radial density distribution correspond to a structured solvation zone consisting of three pronounced solvent shells induced by the PBLG molecule in the surrounding solvent. The figure also shows the radial distribution of the PBLG phenyl rings, illustrating that the helix-induced solvent structure extends well beyond the range of the side chains. Notice also how the phenyl distribution splits into two peaks, whose positions coincide with the corresponding solvent layers, in order to maximize the mixing with the solvent. If one considers the structures solvation shell as an integral part of the PBLG molecule, one obtains an effective diameter of PBLG of ~30 Å. This effective diameter of PBLG in DMF, which is approximately 2 times larger than the interhelical spacing in the solid state (which is about 15.6 Å), correlates well with the effective diameter used in the analysis of recent light scattering experiments.[26] Thus, the question is, how much does the solvation structure contribute to the interaction between the molecules in solution?

First, we employ the above method to measure the force $F_{seg-seg}(t,d(t))$ between two parallel PBG segments (cf. Figure 1A) as a function of their separation d. The resulting intersegment force is shown in Figure 7, where the average PBLG–PBDG center of mass separation d ranges from 7.7 to 22.9 Å.

A discernible onset of the helix–helix interaction can be observed at a distance of about $d \approx 18$ Å, whereas at larger distances $d \gtrsim 19$ Å, the interaction is too weak to be resolved by the simulation. For smaller distances the intersegment force is an overall increasingly repulsive but oscillatory function of the PBG separation. At least three pronounced peaks occur at d = 15.4, 12.6, and 10.6 Å—each indicated by an arrow in Figure 7. Below ~9.5 Å the force increases monotonically, exhibiting a strong repulsion of the closely spaced PBG segments. Note again that there is no attractive PBLG–PBDG interaction over the entire range of investigated helix–helix separations. Notice also that, even though the virtual bonds constrain the relative motion of the two helical backbones to a large extent, there is still sufficient freedom for the possible interdigitation of the "ridges" and "grooves" of the helices, which, however, we do not observe.

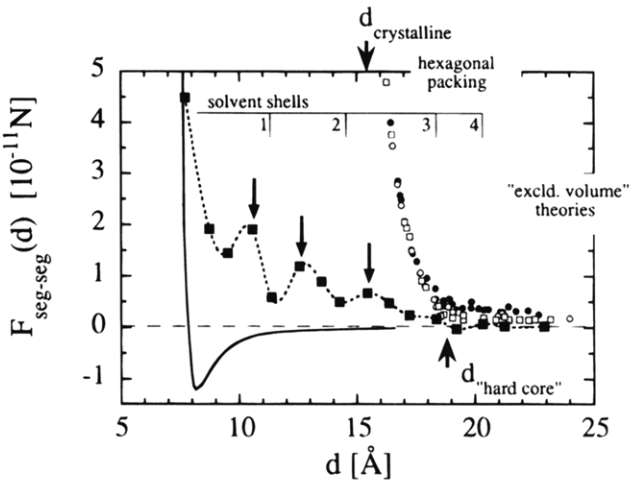

Figure 7. Total intersegment force $F_{seg-seg}(d)$ between two parallel PBG segments in DMF given as a function of the center of mass separation d as obtained from the simulation (■). Pronounced peaks in the force profile are marked by arrows. The numbers in the upper part of the figure indicate the number of DMF solvent shells between the backbones as a function of the helix-to-helix separation. In comparison, van der Waals interaction of two homogeneous cylinders (solid line) and PBG interaction forces estimated from DMF activity data for different molecular length L[7,8] (●, L ~ 1000 Å; ○, L ~ 420 Å; □, L ~ 140 Å).

Before we discuss the force profile in detail, it is useful to briefly discuss the van der Waals interaction of two hollow homogeneous cylinders whose average composition corresponds to that of the backbones of the PBG segments. Thus, the side chains are not considered in this calculation. To describe the van der Waals interaction of two atoms i and j separated by a distance r, which belongs to different cylinders of radius b, we use the 6–12 Lennard-Jones pair potential

$$u(\vec{r}) = \sqrt{\epsilon_i \epsilon_j}\left\{\left(\frac{\sigma_i + \sigma_j}{r}\right)^{12} - 2\left(\frac{\sigma_i + \sigma_j}{r}\right)^{6}\right\} \qquad (15)$$

where ϵ_i and σ_i are the Lennard-Jones parameters of the interacting atoms (cf. eq 2). Here we assume that the atoms or united atoms which form the PBG backbone (i.e., H, O, CH, C, N) are homogeneously "smeared out" over a cylindrical surface enveloping the backbone and that these cylinders interact through effective LJ parameters $\bar{\epsilon}$ and $\bar{\sigma}$, which are calculated by averaging the ϵ_i's and σ_i's according to $\bar{\sigma} = 1/5\sum_{i=1}^{5}\sigma_i$ = 1.61 Å and $\bar{\epsilon} = 1/5\sum_{i=1}^{5}\epsilon_i$ = 0.118 kcal/mol. With this assumption (15) can be written as

$$u(\vec{r}) = \bar{\epsilon}\left\{\left(\frac{2\bar{\sigma}}{r}\right)^{12} - 2\left(\frac{2\bar{\sigma}}{r}\right)^{6}\right\} \qquad (16)$$

The cylinder–cylinder interaction potential per unit length, V_L, is now calculated by integrating (16) over the surfaces of the two cylinders in the limit of an infinite cylinder length, i.e.

$$V_L = \lim_{L\to\infty} \frac{1}{L} n_1 n_2 \int\int u(\vec{r})\, d\vec{r}_1\, d\vec{r}_2 \qquad (17)$$

where $\vec{r}_1$ and $\vec{r}_2$ lie on the surface of the two cylinders, respectively, and the n_i ($i = 1, 2$) are the atomic surface densities. To compare this with the results of the MD simulation, we plot the force $-L\ \partial V_L/\partial d$ in Figure 7, where $L = 27$ Å. The cylinder radius b is treated as a fit parameter adjusted by fitting the divergence of the MD force at $d \lesssim 8$ Å. This yields $b = 3$ Å, which is approximately 1 Å larger than the PBG backbone radius. In contrast to the PBG/DMF simulation result, the van der Waals interaction of the cylinders is purely attractive for $d \gtrsim 8$ Å and, in addition, the interaction range is, of course, much shorter. Even though this approximation is very simplistic, it may serve to illustrate the complexity of the different energetic and entropic interactions involved.

Even though there are no direct measurements of the forces between PBG segments, we can roughly estimate these forces based on solvent activity data obtained in refs 7 and 8 for PBLG at high concentrations. Here we use the approximate thermodynamic relation $\pi(\nu_p) \approx -(RT/V_s)\ \ln(a_s(\nu_p))$ to convert the solvent activity a_s measured as a function of polymer volume fraction ν_p into (osmotic) pressure π. Note that V_s is the molar volume of the solvent. Assuming further that the PBLG molecules are hexagonally packed, the force $F(d)$ acting between two PBLG molecules separated by d roughly can be estimated via $F(d) \approx \pi(Ld/\sqrt{3})$, where L is the length of the PBLG segment and $Ld/\sqrt{3}$ the area of a face of the hexagonal cell (or "honeycomb") thought to surround each PBLG molecule. The experimental separation d is estimated from the polymer volume fraction ν_p via $d \approx d_{cryst}/\sqrt{\nu_p}$, where $d_{cryst} = 15.6$ Å is the crystalline PBLG separation obtained from X-ray studies.[16] The so-obtained "experimental" force is plotted in Figure 7. Remarkably there is a kink in the experimental data, which coincides well with the above-mentioned force threshold at $d \approx 18.5$ Å. For separations less than $d \approx 18.5$ Å the experimental data increase rapidly and, of course, diverge at $d = d_{cryst}$. The molecular weight independent behavior in this region is consistent with our picture of highly aligned molecules. Thus, this behavior suggests that the force onset can be identified with an effective hard-core diameter of the PBG molecule in solution. To understand the quantitative deviation of the experimental data from the simulation result, one should realize that the experimental data are obtained at high PBLG concentration, whereas the simulation considers two single PBG molecules only. Therefore, the free volume available to the side chains in the simulated system is significantly larger than the free volume available in a dense-packed PBG matrix. Finally, notice that for large d the pressure π depends on molecular weight; i.e., the dense packing breaks up and the above approximate relation for the force is no longer valid.

Density and Order Parameter Profiles. As mentioned before, the highly structured solvation zone, which is induced by each single PBG molecule, plays an important role in the PBG–PBG interaction, even though its discernible effect is not as far ranged as inferred from the extension of the radial density variations in Figure 6. In this section we want to take a closer look at the relation between the density variations and the oscillations in the force. In order to do this, we calculate the center of mass density profile of DMF

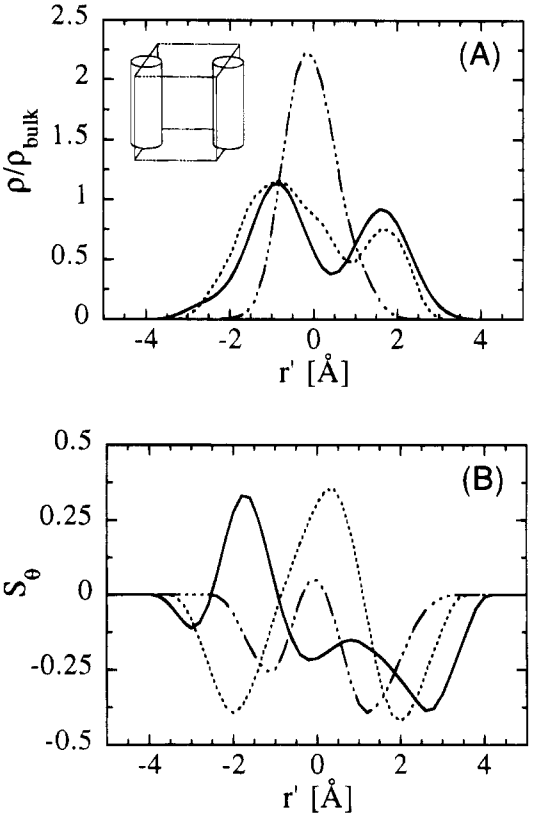

Figure 8. (A) DMF density ϱ divided by the bulk density ϱ_{bulk} in a 6 Å wide slab bounded by the two parallel PBG helices (cf. sketch). The density profiles are for three PBG separations, i.e., $d = 13.6$ Å (solid curve), $d = 12.6$ Å (dotted curve), and $d = 11.4$ Å (dash-dotted curve), in terms of $r' = (r - d/2)$, where r is the perpendicular distance measured from the left helix axis and d is the interhelix separation. (B) Order parameter S_θ again in terms of r' for the same three PBG separations using corresponding line types. Here θ is the angle between the axis perpendicular to the molecular plane of DMF and the helix axis.

across a narrow slab bounded by the helices as shown in the sketch in Figure 8A. The slab is 6 Å wide, which is approximately 2 Å larger than the backbone diameter. In order to focus the discussion on the typical and essential features, we present explicit density profiles only for three distinct helix separations d, which bracket the second force peak in Figure 7.

The three normalized density profiles are shown in Figure 8A for $d = 11.4$, 12.6, and 13.6 Å. The normalization is with respect to the experimental DMF bulk density. For $d = 13.6$ Å the density profile exhibits two well-pronounced peaks representing two distinct solvent layers located between the helices. Compared to the structured solvation zone of a PBLG molecule in DMF as shown in Figure 6, this separation d is approximately twice the radial extension of the first solvent/side-chain shell induced by the isolated molecule. Note that the distances of the layers to the nearest respective helix are ~5.9 and ~5.1 Å, which is close to the radial separation of the first shell induced by the isolated molecule, i.e., ~6 Å. In other words, each molecule contributes its first shell to the profile in Figure 8A. If the PBG separation is reduced by ~1 Å down to 12.6 Å the position of the maxima of the profile (and thus the position of the layers) remain unchanged, which indicates that the solvent molecules are forced to move closer to the helices. Obviously, however, the structure of the two solvent shells is less pronounced and appears slightly "washed out". Compared to the repulsive force

at $d = 13.6$ Å, the repulsion now is increased, suggesting that an additional force is necessary to compress the solvent layers and to disrupt the solvation shell structure. A further decrease of the PBG separation down to 11.4 Å (which is less than twice the radius of the first solvation shell) completely prevents the formation of two distinct solvent layers, and the resulting profile exhibits a single solvent layer only. The repulsion of both PBG molecules, however, decreases again, because the extension of the new structure now is commensurate with the interhelical separation. Note that similar effects are well-known from the solid−liquid−solid interface between flat macroscopic surfaces.[15]

Analogously, we can analyze the solvent profiles for other separations d. The upper part of Figure 7 summarizes the number of interhelical solvent shells as a function of d. At $d = 20.3$ Å four distinct solvent shells are induced in the above-described slab between the segments. A reduction of the separation leads to a compression of the initial four shells, and the number of layers is reduced by one shell at approximately each of the indicated separations, i.e., $d = 18.4$, 14.3, and 11.3 Å.

In addition to the center of mass density profiles, it is interesting to calculate the corresponding solvent orientation order parameter

$$S_\theta = \frac{3\langle \cos^2 \theta \rangle - 1}{2} \tag{18}$$

where θ is the angle between the helix axis and the surface normal of the DMF molecular plane (cf. ref 17). The surface normal is defined by the cross product of the two unit vectors along the two N−CH_3 bonds. Thus, if the DMF molecular plane is oriented parallel to PBG axis, $S_\theta = -0.5$, whereas for the perpendicular orientation, $S_\theta = 1.0$. The DMF order parameter profiles corresponding to the density profiles in Figure 8A are shown in Figure 8B for the same interhelical distances. For $d = 13.6$ Å the molecular planes of the solvent molecules, which are closest to the right helix, are oriented preferentially parallel to the backbone ($S_\theta = -0.35$), whereas the molecules closest to the left helix are tilted away from the helix axis as indicated by a positive order parameter. If the separation is decreased to $d = 12.6$ Å, the molecules change their preferential orientation and the order in the solvent between the helices increases; i.e., the DMF molecular plane in the vicinity of both helices is oriented parallel to the helix axis. Note that the increased orientational molecular ordering is directly correlated with a higher PBLG−PBDG repulsion and, as mentioned before, with a less pronounced double-peak structure of the density profile. A further reduction of the interhelical distance to $d = 11.4$ Å results in a single density peak, which is divided into two regions with different orientational molecular ordering. In spite of the fact that only one layer remains between the two helices, the separate influence of the two PBG molecules is still obvious from the two peaks in the order parameter profile. However, compared to the profile at $d = 12.6$ Å, the solvent molecules mainly keep their preferred orientation, but the resulting order parameter profile is less pronounced and most of the molecules centered between the helices have no preferred orientation. This combined analysis of the density and the order parameter profiles illustrates that the strength of the PBLG−PBDG repulsion is directly correlated with both the shape of the density profile and the molecular orientation of the solvent between the helices.

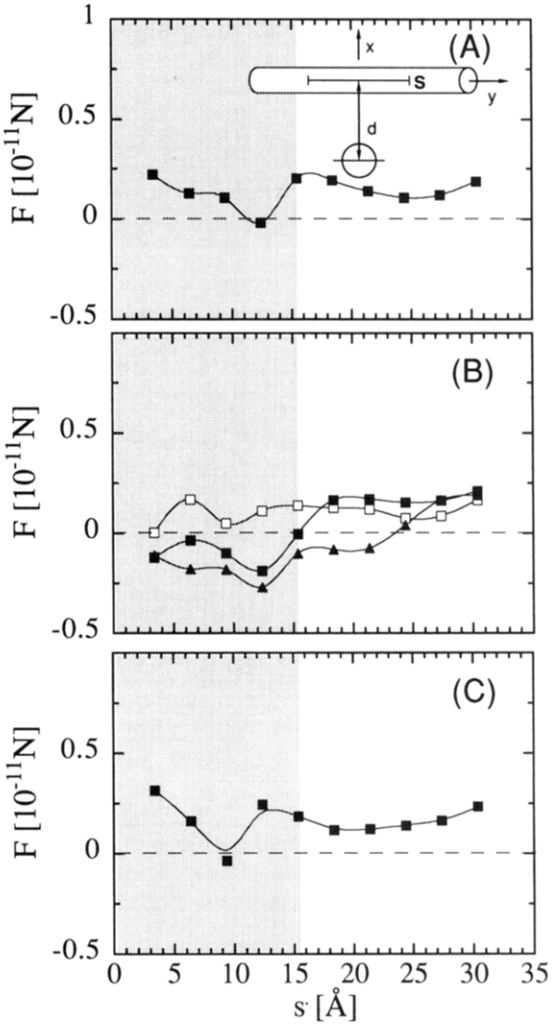

Figure 9. Interaction between two perpendicularly oriented PBLG molecules in DMF. The interaction is given in terms of the total force $F(d)$ acting between backbone sections of length s as a function of s (cf. the sketch in panel A). The forces are shown for five different PBLG separations: (A) $d = 11.3$ Å; (B) $d = 10.3$ Å (□), $d = 9.4$ Å (■), and $d = 8.3$ Å (▲); (C) $d = 7.3$ Å.

3.2. Two Perpendicular PBLG Segments in DMF. To characterize the interaction between two helices oriented perpendicular to each other, we calculate the force between two subsegments on each of the two helices, where each subsegment has the length s (cf. the sketch in Figure 9A). The centers of the two subsegments are separated by d, which is the perpendicular separation between the helices. Figure 9 shows the force $F(d)$ between the subsegments as a function of s for a number of decreasing separations d, i.e., $d = 11.3$, 10.3, 9.4, 8.3, and 7.3 Å. Common to all values of d is that $F(d)$ becomes constant for large s. This is to be expected, because if s is sufficiently large, its additional increase should not affect the interaction between the PBLG segments in the crossed geometry due to the finite range of the interactions. With the exception of $d = 8.3$ Å (panel B) we find that $F(d)$ is roughly constant for values of s exceeding the crystalline diameter of ~15 Å. For smaller s the force $F(d)$ exhibits a more complex behavior. It is worth noting that in this s-region $F(d)$ changes from being overall repulsive for $d = 11.3$ Å (panel A) and $d = 10.3$ Å (panel B) to being overall attractive for $d = 9.4$ and 8.3 Å (panel B) back

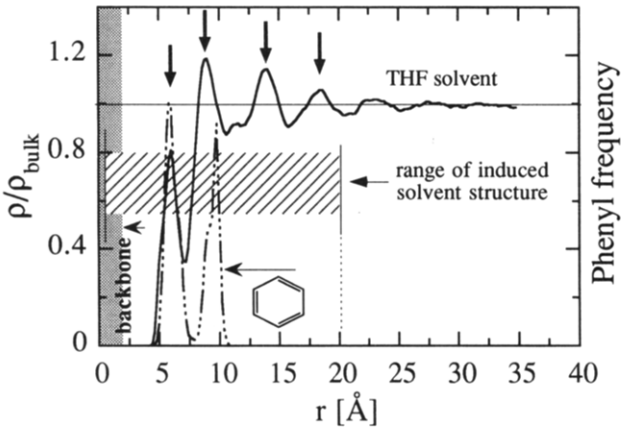

Figure 10. THF density ϱ divided by the bulk density ϱ_{bulk} as a function of the radial distance r from the helix axis (solid line) and radial center of mass distribution of the PBLG phenyl rings (dash-dotted line). The striped horizontal bar indicates the range of the induced solvent structure, which includes of ~4 solvent shells indicated by the arrows.

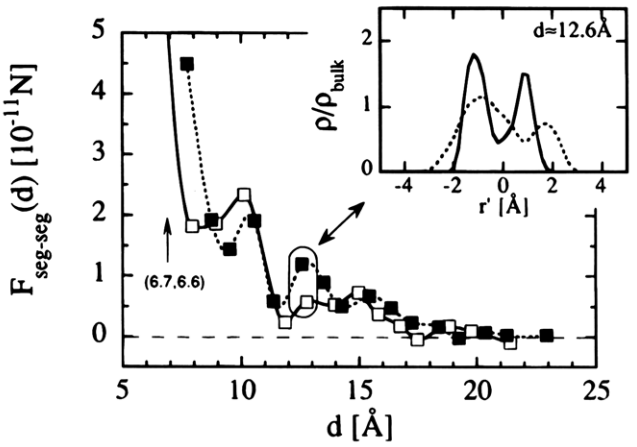

Figure 11. Comparison between interaction of two parallel PBG segments in DMF and THF, respectively. The total force $F_{seg-seg}(d)$ acting between the segments is shown as a function of the interhelix separation d for DMF (■) and THF (□). The inset shows the solvent density profiles for DMF (dotted line) and THF (solid line) when $d \approx 12.6$ Å. The density profile is again calculated in a 6 Å wide slab (cf. the sketch in Figure 8A), where $r' = (r - d/2)$ and r is the distance measured from the left helix axis. The corresponding values of $F(d)$ are highlighted by the oval frame.

to being overall repulsive for $d = 7.3$ Å (panel C). Nevertheless, for large s, i.e., including the entire range over which the helices "feel" each other, the overall interaction remains repulsive as before in the parallel geometry. Note in this context that the interhelical solvent structure is less pronounced because of the small interaction cross section and because the helix-induced solvent shells are "orthogonal" to each other.

3.3. Two Parallel PBG Segments in THF. Before we discuss the force profile of two parallel PBG segments in THF, we give a brief description of the results based on the final 1 ns of a 1.3 ns *NVT* simulation of a single isolated PBLG molecule in THF. Figure 10 shows the center of mass density of THF ϱ as a function of the radial separation r from the helix backbone (i.e., Figure 10 is the analog to Figure 6). Note that the density is normalized to the experimental bulk density of THF ϱ_{bulk}. The density profile exhibits ~4 distinct peaks corresponding to preferred radial positions of the THF molecules. The range of the solvent structure extends out to a distance of approximately ~20 Å from the helix axis, which has to be compared with an extension of ~15 Å in the case of DMF (cf. Figure 6). Note that the peaks in the THF density profile are more pronounced than those in the DMF profile, indicating a higher molecular ordering of the THF molecules in the vicinity of the helix. Taking the induced solvent shells as an integral part of the PBLG molecule, we thus obtain an effective diameter $d \approx 40$ Å for PBLG in THF. As shown in our previous simulation,[17] the molecular structure of DMF in the solvation zone is mainly determined by the two DMF methyl groups; i.e., it is the bulkiness of the $N(CH_3)_2$ group rather than the polar character of the carbonyl group which mainly governs the solvation shell structure. For THF it is again, of course, the size of the molecule which determines the wavelength of the density oscillations, but we might attribute the more pronounced structure to the higher symmetry of the molecule (cf. the similar behavior in the bulk as shown in Figure 3).

Again Figure 10 also shows the extension of the side chains in terms of the radial distribution of the PBLG phenyl rings. As for DMF the side-chain phenyl distribution splits into two peaks at $r \approx 5.5$ and 10 Å, which coincide with the first two solvation shells (even though the second peak lies at the outer periphery of the second solvation shell). Note that the side chains corresponding to the second peak stretch radially away from the backbone and that this behavior is much more pronounced for THF in comparison with DMF (as can be seen from the sharpness and the height of the second peak). Thus, we find a higher degree of side-chain solvation for THF as compared to DMF.

The dependence of the inter-PBG force on the interhelix separation d in THF is shown in Figure 11 together with the result obtained in DMF. The overall behavior is quite similar in both cases. The force in THF, however, is less regularly structured. In particular, there are three noticeably different features in the THF force curve in comparison to the DMF force curve. Whereas the DMF result exhibits an onset of the repulsive interaction at ~19 Å in combination with a steady increase up to about 15 Å, the THF result shows a small "hump" between 18 and 19 Å and a subsequent drop of the force to zero at ~17.5 Å. In addition, the local force maximum at ~12.6 Å in DMF is significantly suppressed in THF. Finally, the divergence of the force at small d is shifted to lower separations for THF.

Analogous to Figure 8A, Figure 11 also compares the solvent density profiles for $d \approx 12.8$ Å calculated in the region between the PBG molecules for the two solvents. In DMF as well as in THF the region between the PBG molecules contains two pronounced solvent layers, which are separated by ~2.7 and ~2.0 Å, respectively. Note again that the lower force in THF corresponds to a density profile which exhibits two well-separated peaks, whereas in the case of DMF the profile is broader and less structured. Interestingly, in spite of the fact that the side chains fold around the backbone in order to minimize the interaction with the opposite PBG molecule, the distance of the THF layers from the helix axis is found to be identical with the separation of the first THF solvation shell induced by a single PBLG molecule with unperturbed side chains, i.e., ~5.3 Å (cf. Figure 10). In contrast, the DMF molecules benefit by the displacement of the side chains and move closer to the backbone as one might expect from the PBLG solvation zone structure (cf. Figure 6). Thus, we assume that the higher repulsion of PBG in DMF results from the different molecular interactions in the region be-

tween the PBG molecules. Especially in the vicinity of the helix, it is the higher dipole moment of DMF μ_{sim} = 3.27 D (in contrast to μ_{sim} = 1.75 D in the case of THF) which causes an increased electrostatic interaction with the highly charged PBG peptide units. Note, in this context, that measurements on PBG samples with a molecular weight of 550 000 suggest a dipole moment of 8000 D measured along the helix axis.[27] If one assumes that the contributions along the axis mainly result from the polar character of the peptide units of the helical backbone, an average dipole moment of ~3.2 D is suggested per peptide unit which is interestingly close to the DMF dipole moment, i.e., μ_{DMF} = 3.27 D. Note also, that based on the calculated peptide charges of the entire simulated PBG segment we obtain dipole moments between ~3.5 and ~4 D per peptide unit calculated along the helix axis, which is in quite good agreement with the experimental data (notice that a straight segment of 27 Å length was analyzed without paying attention to the bending modes, which play an important role for high molecular weight fragments).

4. Conclusions

We have used molecular dynamics simulations to examine the interaction between two helical PBG molecules in DMF and THF. In DMF we study two possible PBLG–PBDG orientations corresponding to a maximum (i.e., parallel segments) and a minimum interaction cross section (i.e., perpendicular segments). In the case of the parallel orientation, the interaction forces are oscillatory functions of the PBG separation and are overall repulsive. Our results show that depending on the PBG separation a distinct number of solvent layers is induced in the intermediate region between the PBG segments and that the solvent structure as well as the molecular orientation is directly correlated with the repulsive forces acting on the PBG segments. We find an effective "hard-core" diameter of ~18.5 Å, which is much smaller than the diameter of the induced solvent structure of about 30 Å but still significantly larger than the intermolecular separation in the crystalline state of about 15.6 Å. The overall interaction between two perpendicular PBLG segments is also repulsive, but we find an attraction of the two segments at PBLG separations between ~9.4 and ~8.3 Å over a certain range along their backbones.

In addition, we analyze the influence of the type of solvent on the PBG–PBG interaction. In THF it appears that the PBG molecules feel a weaker repulsion if they overcome a first barrier, which is also evident from the corresponding interhelical solvent structure. Therefore, from the point of the simulation, an association of PBG in THF seems to be more likely than that in DMF, which is in accord with experimental experience.[28] The type of PBG association (end-to-end or side-by-side) in solvents like THF and dioxane is, however, still unclear (e.g., ref 29). In the case of end-to-end association it appears that solvents like DMF better solvate the PBG ends and thereby prevent this type of association.[29] This work lends support to this idea in terms of the strong dipole–dipole interaction, which is possible between DMF and the exposed peptide units at the ends of the PBG molecule. In other words, in the absence of the bulky side chains the peptide units are effectively screened by the DMF molecules, which suggests the prevention of end-to-end association in DMF.

Acknowledgment. The authors acknowledge several useful discussions with Prof. G. Wegner during the course of this work.

References and Notes

(1) Vroege, G. J.; Lekkerkerker, H. N. W. *Rep. Prog. Phys.* **1992**, *55*, 1241.
(2) Odijk, T. *Macromolecules* **1986**, *19*, 2313.
(3) Odijk, T. *Macromolecules* **1983**, *16*, 1340.
(4) Odijk, T. *Macromolecules* **1984**, *17*, 502.
(5) Podgornik, R.; Parsegian, V. A. *Macromolecules* **1990**, *23*, 2265.
(6) Podgornik, R.; Rau, D. C.; Parsegian, V. A. *Macromolecules* **1989**, *22*, 1780.
(7) Kubo, K.; Ogino, K. *Mol. Cryst. Liq. Cryst.* **1979**, *53*, 207.
(8) Kubo, K. *Mol. Cryst. Liq. Cryst.* **1981**, *74*, 71.
(9) Livolant, F.; Bouligand, Y. *J. Phys. (Paris)* **1986**, *47*, 1813.
(10) Lee, S. D. Thesis, University of Brandeis, Waltham, MA, 1988.
(11) Hentschke, R. *Macromolecules* **1990**, *23*, 1192.
(12) Lee, S. D.; Meyer, R. B. *Liq. Cryst.* **1990**, *7*, 451.
(13) DuPré, D. B.; Yang, S. *J. Chem. Phys.* **1991**, *94*, 7466.
(14) Mathauer, K.; Vahlenkamp, T.; Frank, C. W.; Wegner, G. Poster at the ACS Spring Meeting, Denver, 1993.
(15) Israelachvili, J. *Intermolecular and Surface Forces*, 2nd ed.; Academic Press: New York, 1992.
(16) Bamford, C. H.; Elliot, A.; Hanby, W. E. *Synthetic Polypeptides*; Academic Press: New York, 1956.
(17) Helfrich, J.; Hentschke, R.; Apel, U. M. *Macromolecules* **1994**, *27*, 472.
(18) Techniques of Chemistry. *Organic Solvents*, 4th ed.; John Wiley & Sons: New York, 1986; Vol. II.
(19) Allen, M. P.; Tildesley, D. J. *Computer Simulation of Liquids*; Oxford University Press: Oxford, U.K., 1992.
(20) Weiner, S. J.; Kollman, P. A.; Nguyen, D. T.; Case, D. A. *J. Comput. Chem.* **1986**, *7*, 230.
(21) Rappé, A. K.; Goddard, W. A. *J. Phys. Chem.* **1991**, *95*, 3358.
(22) POLYGRAF Version 3.2.1, Molecular Simulations Inc., 1993.
(23) van Gunsteren, W. F.; Berendsen, H. J. C. *Mol. Phys.* **1977**, *34*, 1311.
(24) Berendsen, H. J. C.; Postma, J. P. M.; van Gunsteren, W. F.; DiNola, A.; Haak, J. R. *J. Chem. Phys.* **1984**, *81*, 3684.
(25) v. Goldammer, E.; Zeidler, M. D. *Ber. Bunsen-Ges. Phys. Chem.* **1969**, *73*, 4.
(26) Schmidt, M. *Macromolecules* **1984**, *17*, 553.
(27) Levine, B. F.; Bethea, C. G. *J. Chem. Phys.* **1976**, *65*, 1989.
(28) Bruhn, C. Personal communication.
(29) Doty, P.; Bradbury, J. H.; Holtzer, A. M. *J. Am. Chem. Soc.* **1956**, *78*, 947.

MA9462013